Original Article

INNOVATIVE APPROACH: MRI-GUIDED FABRICATION OF A BIOMIMETIC INTERVERTEBRAL DISC SCAFFOLD

Y.C. Ye[1,2,§], C. Shao[1,§], Y. Wang[3], F.G. Lin[1], P. Su[1], Y.P. Niu[1], H.W. Yang[2], Z.C. Wang[2], T. Ma[2], S. Ji[2], W.J. Chang[1,2], J. Xi[4], R. Wang[4], K. Zhu[2,*], C.C. Zhang[2,*] and Y.M. Sun[1,*]

[1]Department of Orthopedics, The Second Affiliated Hospital of Soochow University, 215000 Suzhou, Jiangsu, China
[2]Department of Orthopedics, The First Affiliated Hospital of Bengbu Medical University, 233004 Bengbu, Anhui, China
[3]Department of Orthopedics, The First People's Hospital of Lianyungang, 222000 Lianyungang, Jiangsu, China
[4]Anhui Province Key Laboratory of Tissue Transplantation, Bengbu Medical University, 233030 Bengbu, Anhui, China
[§]These authors contributed equally.

Abstract

Background: This study aimed to develop a new intervertebral disc (IVD) scaffold using magnetic resonance imaging (MRI) grayscale image analysis and gray exposure digital light processing (GE-DLP) technology to replicate the natural structure of the IVD, providing improved biomechanical performance and cell compatibility. Tissue engineering presents a promising alternative, with bio-scaffolds being a key element for IVD regeneration. **Methods**: In this study, a three-dimensional (3D) model of the IVD was constructed from MRI scans of a healthy volunteer, and the grayscale images were processed to distinguish between tissue types. Exposure times were adjusted based on grayscale values, and GE-DLP was employed to fabricate the biomimetic IVD scaffold in a single integrated process using a bicomponent polymer network (BCN) hydrogel laden with nucleus pulposus mesenchymal stem cells (NPMSCs). The microstructure and porosity of the scaffold were analyzed using scanning electron microscopy (SEM), and the elastic modulus across the radial distribution was evaluated by nanoindentation. In addition, the biomechanical performance was determined using finite element analysis (FEA). For biocompatibility assessment, cytoskeleton staining was conducted to observe cell morphology, and cell viability was evaluated using Calcein/propidium iodide (PI) staining. **Results**: The biomimetic IVD scaffold mimicked the natural structure and mechanics of the intervertebral disc, with gradient changes in elastic modulus and pore size. Finite element analysis showed that the scaffold responded similarly to a real IVD during certain movements. Scanning electron microscopy showed a network of pores in the scaffold that are important for cell attachment and growth. The scaffold showed high biocompatibility, with cells surviving well for seven days. **Conclusions**: In this research, a novel biomimetic IVD scaffold with excellent static structural integrity and biomechanical performance was successfully engineered by combining MRI image analysis and GE-DLP technology.

Keywords: Intervertebral disc (IVD), magnetic resonance imaging (MRI), 3D biomanufacturing, hydrogel, finite element analysis (FEA).

***Address for correspondence**: Y.M. Sun, Department of Orthopedics, The Second Affiliated Hospital of Soochow University, 215000 Suzhou, Jiangsu, China. Email: ymingsun@126.com; C.C. Zhang, Department of Orthopedics, The First Affiliated Hospital of Bengbu Medical University, 233004 Bengbu, Anhui, China. Email: zccanhui1968@126.com; K. Zhu, Department of Orthopedics, The First Affiliated Hospital of Bengbu Medical University, 233004 Bengbu, Anhui, China. Email: zk19870128@163.com.

Introduction

The intervertebral disc (IVD) is an essential component of the spinal column that supports mechanical loads, preserves spinal stability, and enables mobility [1,2]. Damage or degeneration of the IVD significantly impacts the quality of life, which may lead to back and neck pain, and place substantial strain on healthcare resources [3].

Current treatments for IVD include medication, physical therapy, and surgery; however, these therapeutic modalities only provide temporary relief but do not address the root cause. Research is now focusing on new therapies to restore or replace damaged IVDs [4,5]. In the realm of tissue engineering, bio-scaffolds have been thoroughly investigated and employed as a crucial component in facilitating IVD regeneration. An optimal IVD bio-scaffold should demonstrate high biocompatibility, appropriate porosity, mechanical characteristics, and the ability to mimic the natural gradient structure of the IVD [6,7].

IVD tissue is a viscoelastic, nonlinear, and anisotropic disc-shaped entity that can be divided radially from the interior to the exterior into three primary hierarchical components: nucleus pulposus (NP), inner annulus fibrosus (IAF), and outer annulus fibrosus (OAF) [8]. The varying composition and characteristics of the extracellular matrix in different regions create an ideal environment for cells, influencing their behavior and tissue regeneration. Therefore, accurately creating a biomimetic gradient bio-scaffold that replicates the structure and elasticity of the intervertebral disc is crucial for repairing and regenerating disc tissue [9–11].

Currently a variety of biomaterials and polymer scaffolds have been developed and applied to cell-based engineered annulus fibrosus (AF) and NP tissues, as well as to them as a combination of overall disc structures [10,12]. For example, some investigator studies have attempted to promote organized AF-like tissue using self-organizing collagen-based gels, layered nanofiber scaffolds, or mesh scaffolds composed of silk proteins, or acellular mesh scaffolds for AF [13–15]. Others have wrapped cells in a variety of hydrogels, including agarose, fibrin/hyaluronic acid (HA), carboxymethyl cellulose, or alginate gels, to generate NP-like tissue structures [16–20]. More and more researchers are combining these different scaffolds to reconstruct the entire IVD in engineered composites. Choy *et al*. [21] prepared a biphasic scaffold with structure and function using collagen and glycosaminoglycan. Kim *et al*. [22] fabricated disc-like angle ply structures for total disc arthroplasty, including polycaprolactone (PCL) electrospun nanofibers AF and HA hydrogel core NP. Despite the promise of these engineered discs, we noticed poor cell penetration and migration in these scaffolds, and a lack of effective transition zones and junctions between NP and AF.

Magnetic resonance imaging (MRI) is a non-invasive imaging modality with exceptional soft tissue contrast and has emerged as a pivotal tool for investigating the internal structure and functionality of the intervertebral disc. In particular, MRI grayscale images can provide detailed information on the pore structure and connectivity of a scaffold, playing an indispensable role in the design and fabrication of bio-scaffolds [23].

Gray exposure digital light processing (GE-DLP) technology accurately projects grayscale image slices onto a hydrogel precursor to create three-dimensional (3D) structures [24,25]. After printing, the hydrogel is submerged in water to create localized heterogeneity through gradient crosslinking density. The mesh size and microphase separation can be adjusted to customize the pattern, resulting in varied local light transmittance [26,27]. Hence, intricate internal structures can be produced using a layer-by-layer 3D printing approach. GE-DLP technology enables the precise replication of microstructures, yielding a cohesive IVD scaffold.

This study aimed to develop a new method for creating gradient IVD bio-scaffolds by combining MRI images with DLP technology. MRI data were used to control scaffold porosity and pore size, mimicking the natural structure of the IVD and enhancing its biomechanical properties and cell compatibility. The study employed finite element analysis (FEA) to assess the biomechanics of the bio-scaffolds, which were produced using cell-loaded 3D printing techniques. The biomechanical functionality of 3D hydrogel scaffolds with nucleus pulposus mesenchymal stem cells (NPMSCs) was improved by optimizing their gradient structure to achieve a uniform cell distribution and growth. Our comprehensive assessment of biocompatibility provided enhanced scaffold evaluation, thereby contributing to the advancement of IVD scaffold design. In summary, a connection is expected between biocompatibility tests and FEA findings, enhancing scaffold evaluation and informing IVD tissue engineering design.

Materials and Methods

Material Selection and Hydrogel Ink Preparation

In this research, a bicomponent polymer network (BCN) hydrogel, previously validated for its biodegradability and exceptional biocompatibility, was chosen [28,29]. A mixture of 10 wt % gelatin methacrylate (GelMA) solution and 1 wt % hyaluronic acid methacrylate (HAMA) at a 10:1 volume ratio was prepared at room temperature and placed in a cell culture dish. A 0.5 wt % photoinitiator (lithium phenyl-2,4,6-trimethylbenzoylphosphinate) was added as a dispersing agent. The mixture was exposed to 405 nm ultraviolet (UV) light for 30 s, followed by curing. The hydrogel was removed from the dish, rinsed with phosphate buffered saline (PBS), and stored for further use.

Extraction and Culture of NPMSCs

Following established protocols, healthy Sprague Dawley rats weighing 200–220 g were euthanized by intraperitoneal injection of phenobarbital sodium solution. The IVD was harvested from the tail of the rat, and gelatinous NP tissue was isolated. The tissue was then washed three times with PBS supplemented with 1 % penicillin-streptomycin, followed by digestion with a 0.2 % solution of Type II collagenase (Gibco, Waltham, MA, USA, Batch No.: 6124412) at 37 °C for 2 h. Following centrifugation at 100 × g for 5 min, the sedimented cell clumps were transferred to a mesenchymal stem cell medium supplemented with 20 % fetal bovine serum (Hyclone, Logan, UT, USA, Batch No.: SLCP22723V) and 1 % penicillin/streptomycin (Invitrogen, Carlsbad, CA, USA, Batch No.: 2585619) and cultured at 37 °C and 5 % CO_2 in a humidified incubator. After 24 h of culture, the medium containing the suspended cells was removed and replaced twice a week. The cells were cultured until the third passage, and the cells from the third passage were used in subsequent experiments, with the mycoplasma test result being negative (procedures for the

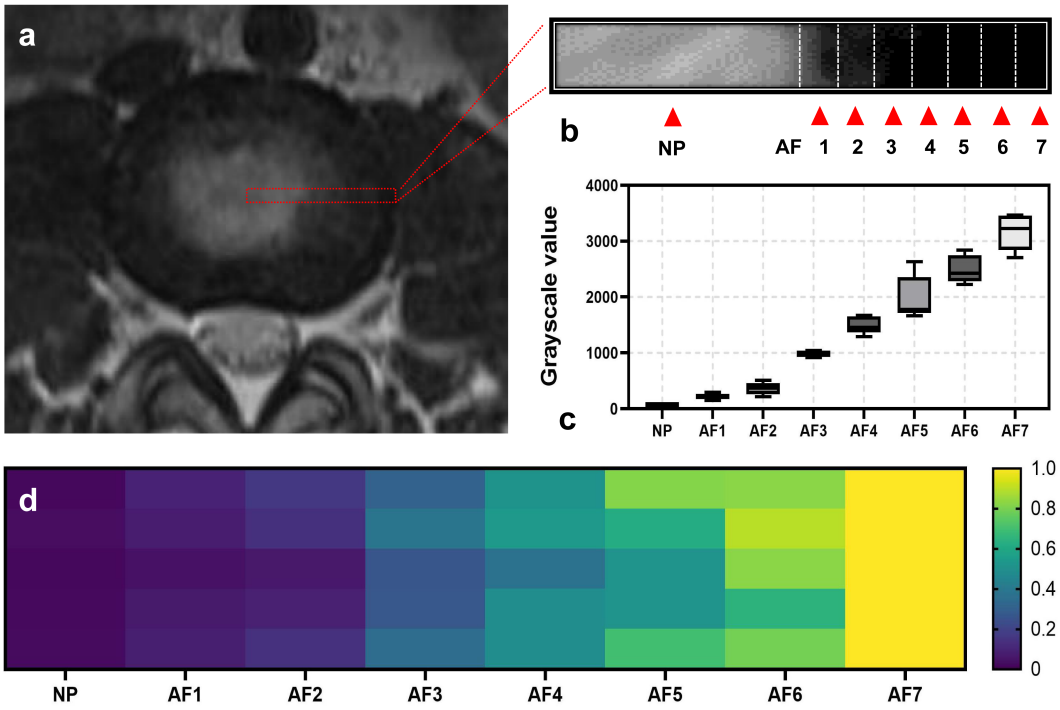

Fig. 1. Lumbar disc magnetic resonance (MR) gray level analysis and exposure intensity encoding assignment. (**a**) The original lumbar disc MR image is used, with radial strip images taken from the center of the nucleus pulposus (NP) to the outermost edge of the annulus fibrosus (AF), followed by hierarchical segmentation into the NP region and the AF 1–7 regions (**b**). (**c**) The gray level analysis is repeated four times to obtain the average gray level value for each region. (**d**) Based on the specific data of the gray level values, an inversion is performed to obtain reference values for exposure intensity. This image was produced using ImageJ and GraphPad Prism software.

identification of relevant NPMSCs are described in **Supplementary Materials S1–S3**).

3D Model Construction

A healthy adult male volunteer underwent an MRI scan using a 3.0 T scanner to obtain the original grayscale image of the intervertebral disc. The scanning parameters were set as follows: repetition time/echo time, 2500/90 ms; field of view, 120 × 120 mm²; matrix size, 512 × 512; and slice thickness, 1 mm. The L4–L5 segment of the patient's MRI image was imported into Mimics 21.0 software (Leuven, Belgium) for 3D model reconstruction and stratification of the nucleus pulposus and annulus fibrosus. Solid surface reconstruction was conducted using Geomagic Studio 12 (Rock Hill, SC, USA), followed by smoothing with creo 8.0 software (Needham, MA, USA) to establish a 3D numerical model of the intervertebral disc tissue structure.

Grayscale Image Processing and Three-Dimensional Biofabrication

Preprocessed MRI images were analyzed using grayscale encoding to differentiate among various tissues within the intervertebral disc, including the nucleus pulposus and annulus fibrosus. Based on the grayscale values, the corresponding biomechanical parameters were assigned to different tissues. The MRI grayscale image data and biomechanical parameters were imported into FEA software to establish a three-dimensional geometric model of the intervertebral disc. Grayscale images reflecting the density and structural information of the intervertebral disc were transformed and extracted. Using grayscale exposure technology, also known as the GE-DLP technique, the exposure intensity was adjusted according to the grayscale value of the digital light masks, allowing precise control of photopolymerization during the 3D printing process. The processed grayscale images were used to reconstruct the three-dimensional model of the intervertebral disc using im-

age processing software, involving threshold segmentation, edge detection, and region-growth techniques. Finally, the reconstructed 3D model was imported into a 3D printer, using the BCN hydrogel laden with NPMSCs as the printing ink to fabricate the intervertebral disc model.

Scanning Electron Microscopy and Porosity Measurement

The morphology and microstructure of various regions of the IVD bio-scaffold were analyzed using scanning electron microscopy (SEM). The scaffolds were coated with a thin layer of gold via sputtering to enhance the image contrast and reduce charging effects during SEM observation. High-resolution SEM images of both the surface and cross-sectional areas were obtained to provide detailed insight into the microarchitecture of the scaffold [30,31].

Subsequently, the porosity of the scaffolds (n = 3) was quantified by analyzing the SEM images using image analysis software (ImageJ, Bethesda, MD, USA, Version No. 12.0.6). The ratio of pore area to total area within the scaffold was determined, thereby calculating the percentage of porosity. Accurately measuring porosity is crucial for assessing the suitability of a scaffold for cell infiltration, nutrient exchange, and tissue integration, which are essential factors for IVD regeneration.

Nanoindentation Test

The elastic modulus and hardness of the printed scaffold materials (n = 5) were evaluated by nanoindentation tests. An MTS Nano Indenter® XP (Eden Prairie, MN, USA, Batch No.: 145265) was used to perform indentation tests on eight different areas of the scaffold material, with at least five indentations per area to ensure data reliability. The obtained elastic modulus values were imported into a previously established 3D finite element model for further biomechanical analysis.

Finite Element Analysis

The mechanical properties of the bioscaffolds were further validated using a finite element analysis. The L4–L5 segment of the intervertebral disc was subjected to various flexion angles (flexion, 4.65°; extension, 10.5°; left rotation, 1.5°; left lateral bending, 6°), as described in the literature [32]. A finite element grid model of the L4–L5 intervertebral disc was established using the ANSA software (Farmington Hills, MI, USA, v25.1.1), with boundary conditions and loads defined using ABAQUS (Providence, RI, USA, v2024). All preprocessing was completed using ANSA, and the ABAQUS/standard implicit solver was used for solving. The results were analyzed using the ABAQUS post-processing viewer.

Cell Viability/Cytotoxicity Assay

The hydrogel scaffolds cultured with NPMSCs were washed with PBS to remove any substances from the culture medium that could interfere with staining. Live (Calcein acetoxymethyl (Calcein-AM)) and dead (propidium iodide (PI)) cell dyes were prepared at appropriate concentrations. After staining, the cells were washed again with PBS to remove unbound dye. PBS or an anti-fluorescence quenching agent was added and the cells were sealed to reduce fluorescence decay. Laser confocal microscopy was used to observe and analyze fluorescence signals, with green fluorescence indicating live cells and red fluorescence indicating dead cells.

Cytoskeleton Staining

The cells were placed in a scaffold for 3D culture at an appropriate density and fixed with 4 % formaldehyde for 20 min. After fixation, cells were washed with PBS to remove residual fixative. Cells were permeabilized with 0.1 % Triton X-100 to enhance phalloidin penetration. The cells were then stained with fuorescein isothiocyanate (FITC)-labeled phalloidin or other fluorescently labeled phalloidins for 30–60 min at room temperature. After staining, the cells were washed with PBS to remove unbound phalloidin. Subsequently, 4′,6-diamidino-2-phenylindole (DAPI) was used to stain the cell nuclei, allowing the simultaneous observation of the cytoskeleton and nuclei. Finally, fluorescence images of the cytoskeleton were captured using a confocal microscope.

Statistical Analysis

All experiments were performed in triplicate or more ($n \geq 3$). Data are presented as mean ± standard deviation (SD). Statistical analysis was conducted using the SPSS software (IBM Corporation, Armonk, NY, USA, v29.0) with one-way analysis of variance (ANOVA) and Tukey's multiple comparison test to evaluate the significance of differences between groups.

Results

Processing and Analysis of Raw MRI Gray-Scale Images

After preprocessing, the MRI images were subjected to meticulous grayscale encoding analysis to differentiate various tissue types within the intervertebral disc, such as the nucleus pulposus and annulus fibrosus (Fig. 1**a**). Consequently, biomechanical properties were assigned to each tissue type, including the nucleus pulposus region and annulus fibrosus, based on the grayscale values (Fig. 1**b**). The annulus fibrosus was radially stratified into seven layers, corresponding to the gradient of the gray-scale value changes. In addition, ImageJ software was used to analyze and extract grayscale values from each stratum of the original intervertebral disc MRI images. Specific data are presented in Fig. 1**c**, demonstrating a gradient change in the grayscale image of the intervertebral disc radially. Ultimately, the exposure intensity for the corresponding areas was deduced by reverse calculation based on the statistical conditions of the grayscale values (Fig. 1**d**).

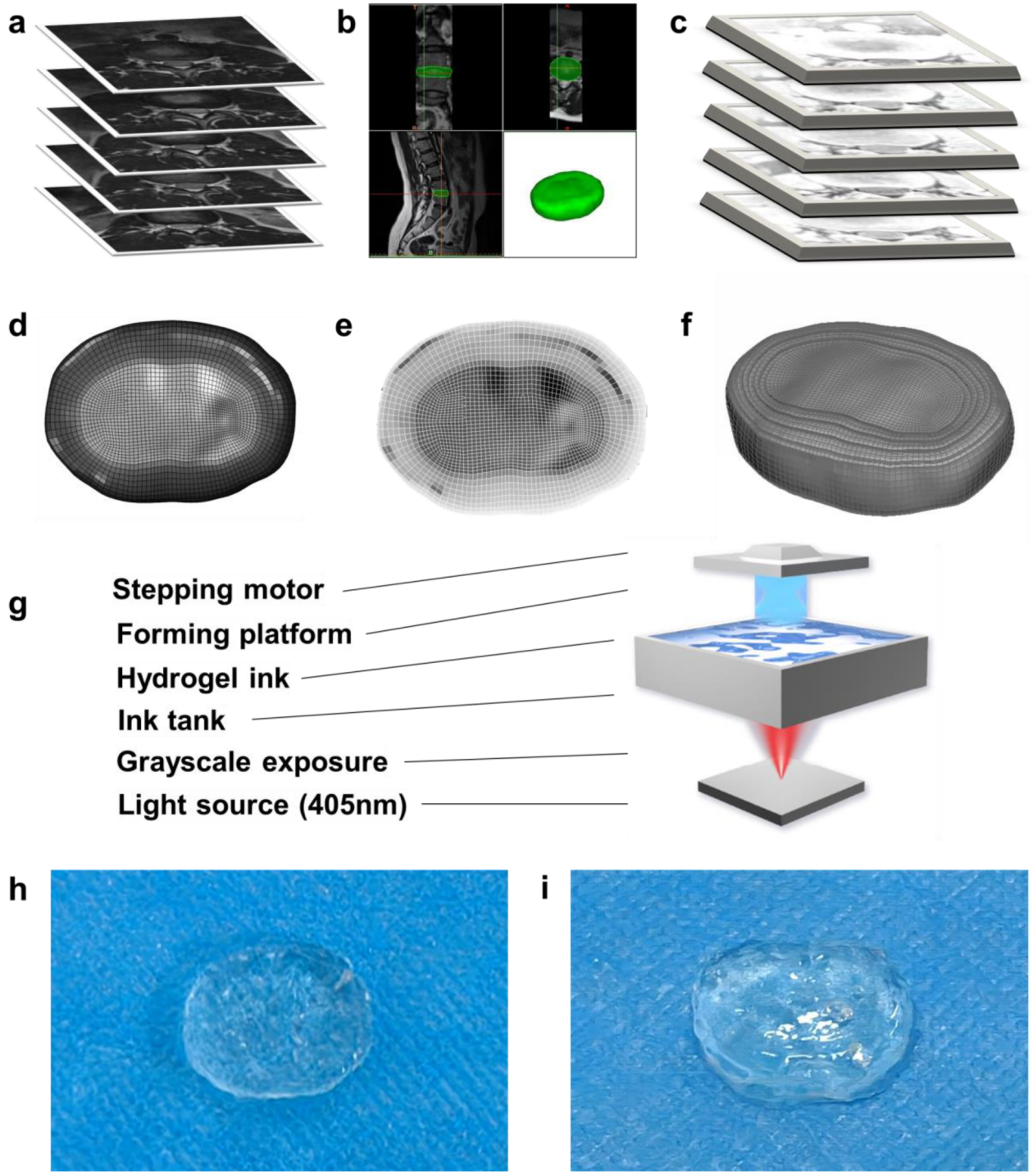

Fig. 2. Construction of a biomimetic lumbar disc scaffold using combined MRI and GE-DLP. (**a**) The original magnetic resonance tomographic images of the lumbar disc. (**b**) Preliminary modeling is conducted using Mimics software based on the three-dimensional imaging from the magnetic resonance. (**c**) The original images are inverted to simulate the printing images of the reagent GE-DLP. (**d–f**) The distribution of mesh division, Image invert and schematic diagram of the three-dimensional model after the modeling is completed. (**g**) Schematic diagram of the GE-DLP device structure. (**h,i**) The general form of the biomimetic lumbar disc hydrogel spacer after 3D printing is formed (top view and oblique view of scaffold). This image was produced using Materialise Mimics and Adobe Illustrator software. MRI, magnetic resonance imaging; GE-DLP, gray exposure digital light processing; 3D, three-dimensional.

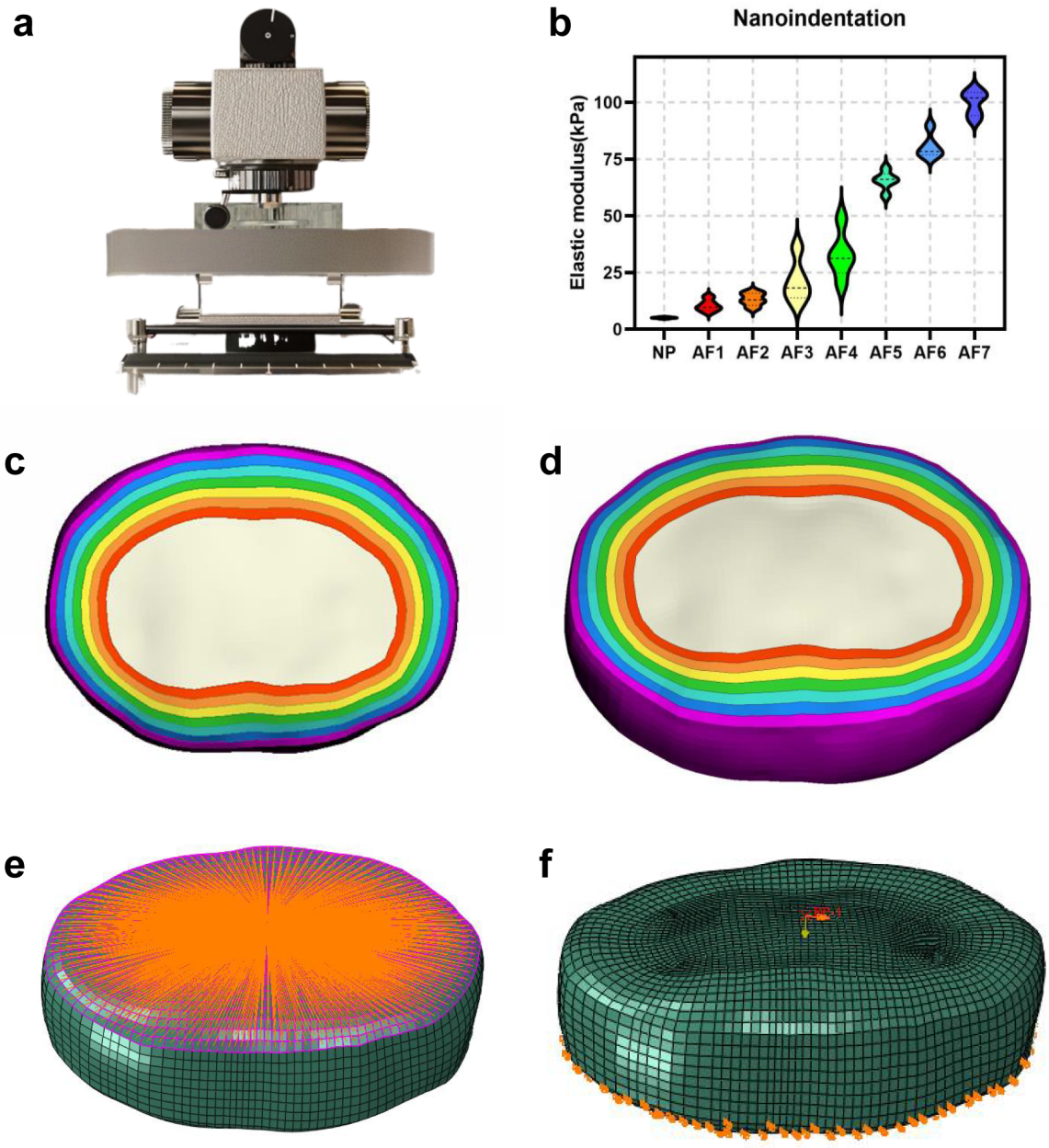

Fig. 3. Threshold segmentation and material assignment of the three-dimensional finite element model. (**a,b**) The elastic modulus values of each hierarchical structure of the constructed biomimetic scaffold are obtained using a nanoindentation instrument. (**c,d**) The regional division and material assignment of the NP region and the AF 1–7 layers (top view and oblique view 3D model). (**e,f**) To facilitate the loading of mobility, a coupling point is established at the center of the upper surface of the intervertebral disc, and the upper surface is coupled, with the bottom disc being fixed. Six types of condition analysis, including anterior flexion, posterior extension, left rotation, and left lateral bending, are applied to the reference point structure on the upper part of the intervertebral disc. This image was produced using ANSA, Adobe Illustrator and GraphPad Prism software.

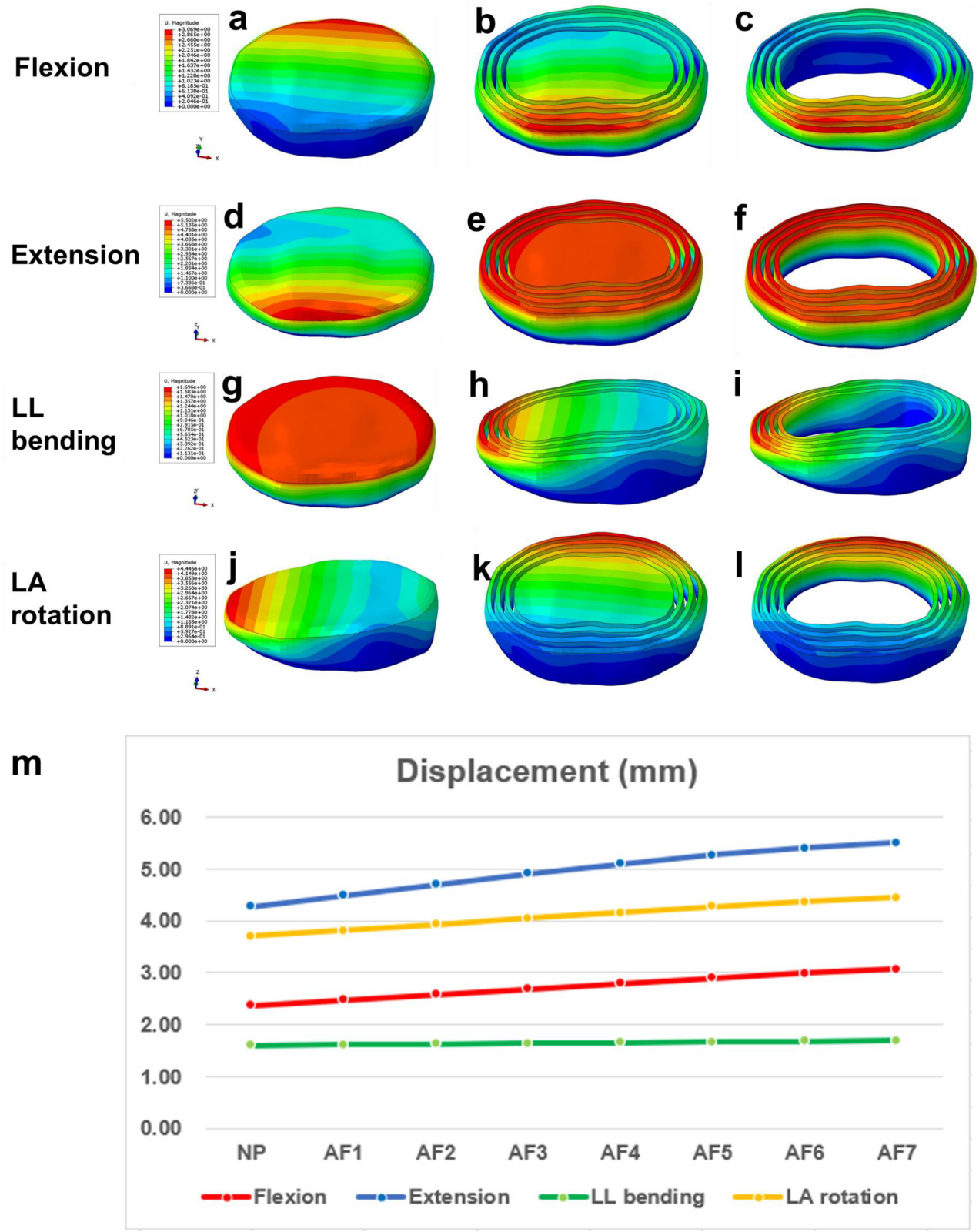

Fig. 4. Displacement testing and statistical charts of the biomimetic intervertebral disc spacer. (**a–c**) Distribution charts of displacement values in the biomimetic spacer under the anterior flexion condition. (**d–f**) Distribution charts of displacement values in the biomimetic spacer under the posterior extension condition. (**g–i**) Distribution charts of displacement values in the biomimetic spacer under the left lateral bending condition. (**j–l**) Distribution charts of displacement values in the biomimetic spacer under the left rotation condition. (**m**) Statistical chart of displacement values under various conditions. All tests were conducted three times. This image was produced using ANSA and Origin software. LL, left lateral; LA, left axial.

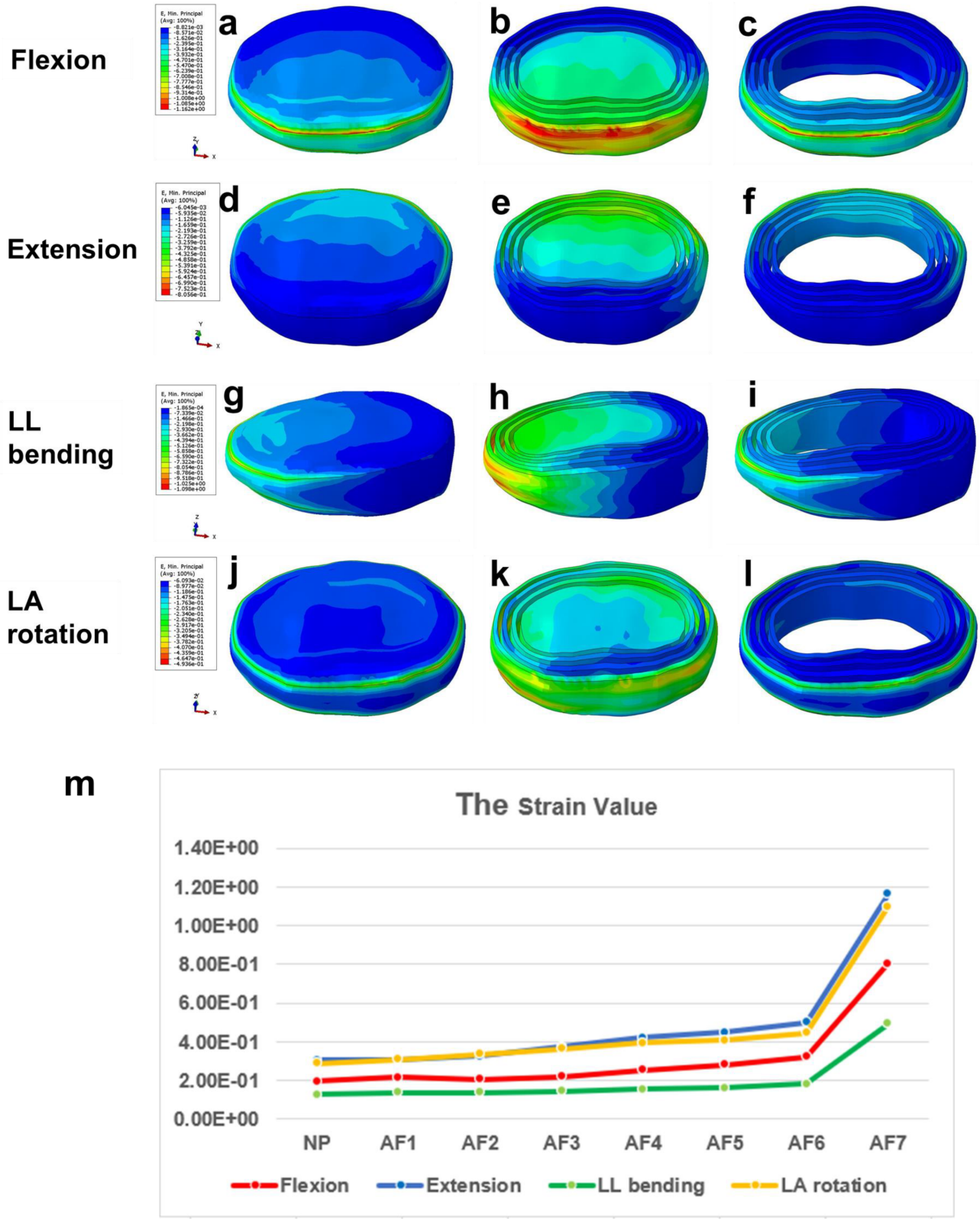

Fig. 5. Strain testing and statistical charts of the biomimetic intervertebral disc scaffold. (**a–c**) Distribution charts of strain values in the biomimetic spacer under the anterior flexion condition. (**d–f**) Distribution charts of strain values in the biomimetic spacer under the posterior extension condition. (**g–i**) Distribution charts of strain values in the biomimetic spacer under the left lateral bending condition. (**j–l**) Distribution charts of strain values in the biomimetic spacer under the left rotation condition. (**m**) Statistical chart of strain values under various conditions. All tests were conducted three times. This image was produced using ANSA and Origin software.

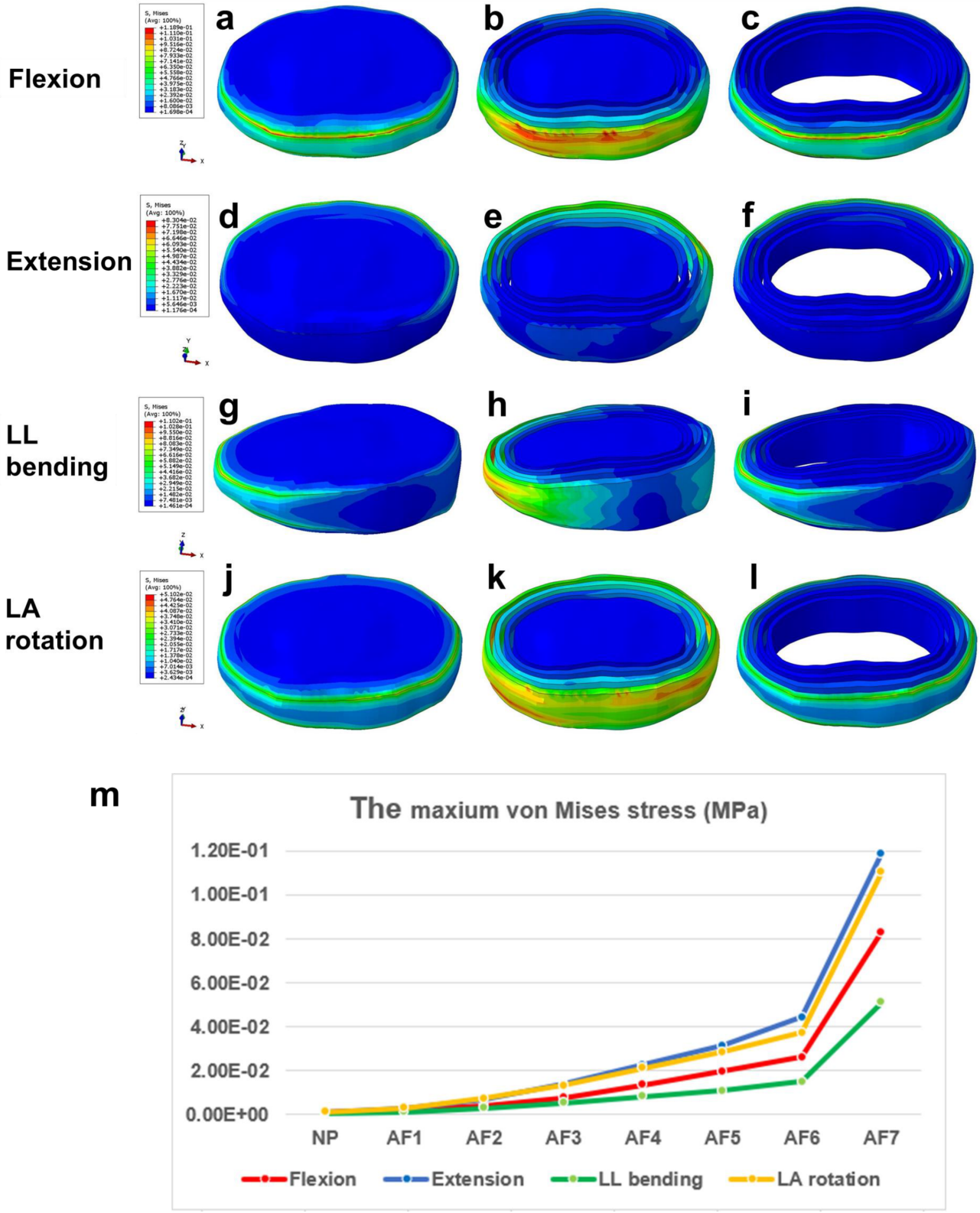

Fig. 6. Stress testing and statistical charts of the biomimetic intervertebral disc scaffold. (**a–c**) Distribution charts of stress values in the biomimetic spacer under the anterior flexion condition. (**d–f**) Distribution charts of stress values in the biomimetic spacer under the posterior extension condition. (**g–i**) Distribution charts of stress values in the biomimetic spacer under the left lateral bending condition. (**j–l**) Distribution charts of stress values in the biomimetic spacer under the left rotation condition. (**m**) Statistical chart of stress values under various conditions. All tests were conducted three times. This image was produced using ANSA and Origin software.

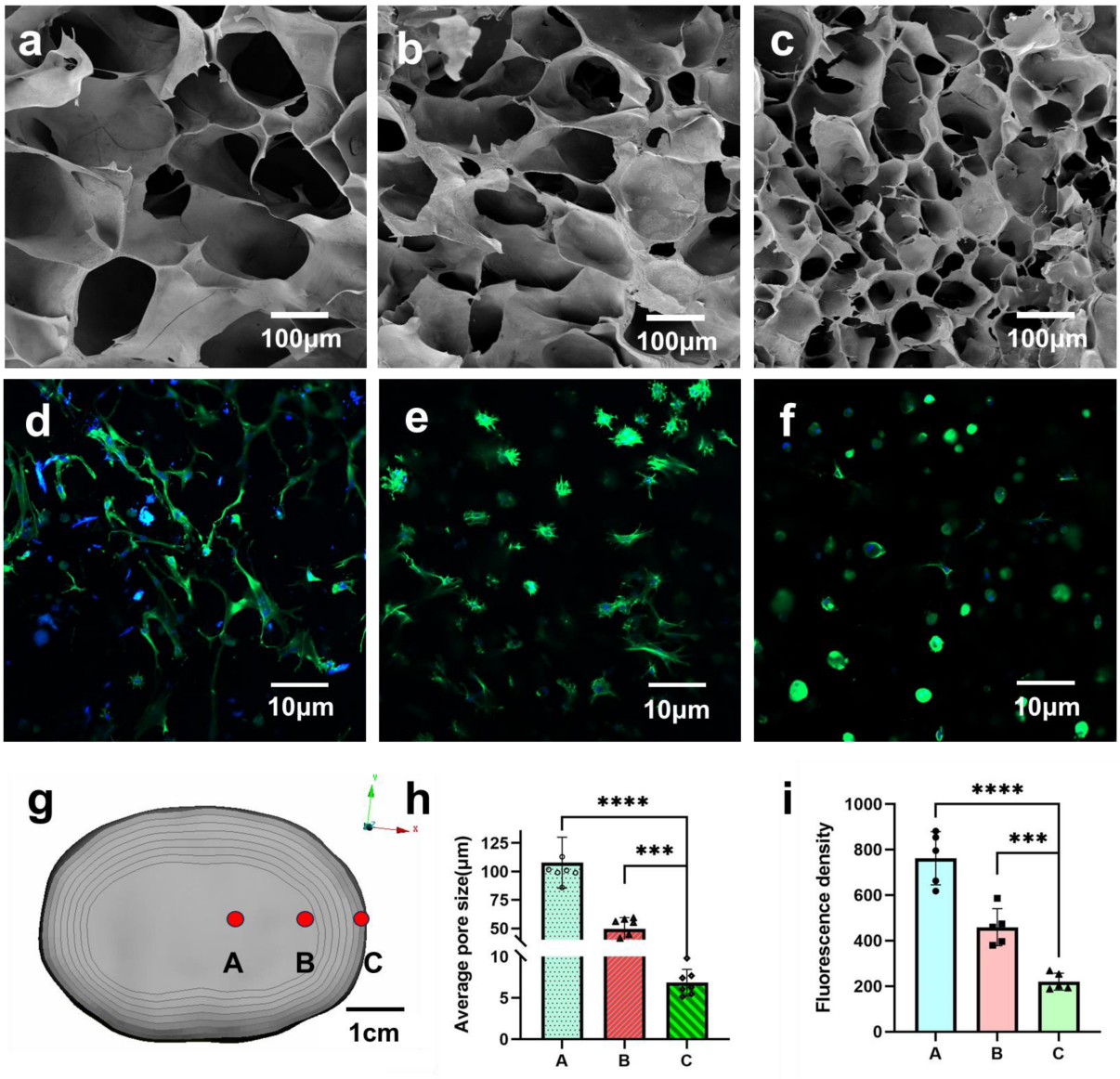

Fig. 7. Microscopic morphology of the intervertebral disc spacer and cell skeleton staining. (**a–c**) Scanning electron microscopy (SEM) images of three points on the radial inner, middle, and outer parts of the bio-scaffold (scale bar: 100 μm). (**d–f**) Cell skeleton staining images of three points on the radial inner, middle, and outer parts of the bio-scaffold (scale bar: 10 μm). (**g**) Schematic diagram of point selection marking (scale bar: 1 cm). (**h**) Statistical chart of pore size at points A, B, and C. (**i**) Statistical chart of fluorescence density at points A, B, and C. All tests were conducted three times. Symbols representing significance levels are indicated as follows: ***$p < 0.001$, and ****$p < 0.0001$. This image was produced using GraphPad Prism software.

Construction of Hydrogel Scaffolds Based on GE-DLP Technology

Using GE-DLP technology, the 3D model was converted into a series of 2D slices using slicing software, which were utilized for 3D printing (Fig. 2**a–c**). The exposure intensity required for the intervertebral disc scaffold during the photopolymerization process was set according to the grayscale values obtained from the previous steps (Fig. 2**d–f**). During the DLP printing process, the light of the corresponding intensity was adjusted and reflected based on the gray-scale value of each pixel point using the digital micromirror device (DMD) or corresponding light modulation device. Areas with higher gray-scale values received stronger light intensity, resulting in higher crosslinking density and mechanical properties. Therefore, the mechanical properties of the printed hydrogel scaffolds demonstrated a gradual change radially from the outside to the inside, mimicking that of natural IVD tissues (Fig. 2**g**). After molding, the overall shape accurately replicated that of the human intervertebral disc (Fig. 2**h,i**).

Table 1. Experimental data of nanoindentation in different zones between intervertebral discs.

Region	Elastic modulus (kPa)					
	Point 1	Point 2	Point 3	Point 4	Point 5	Mean ± standard deviation
NP	4.92	5.13	4.63	5.03	5.36	5.014 ± 0.24
AF 1	9.23	11.56	14.33	7.63	9.69	10.488 ± 2.29
AF 2	12.96	9.37	11.85	16.51	15.31	13.2 ± 2.53
AF 3	18.19	35.96	23.66	11.58	16.22	21.122 ± 8.37
AF 4	31.23	48.69	29.34	20.32	34.96	32.908 ± 9.24
AF 5	59.03	65.06	66.08	66.22	70.79	65.436 ± 3.76
AF 6	78.33	89.65	77.36	76.33	81.36	80.606 ± 4.82
AF 7	92.36	105.7	101.97	102.99	95.99	99.802 ± 4.89

NP, nucleus pulposus; AF, annulus fibrosus.

Material Assignment in the Finite Element Three-Dimensional Model

Using the aforementioned methods, the elastic moduli of eight different layers within the intervertebral disc scaffold were obtained by nanoindentation testing (Table 1). The obtained elastic modulus values were input into the previously established three-dimensional finite element model (Fig. 3**a,b**). Thereafter, the discus grid model was established using the ANSA software with a total of 17,504 elements, including 17,472 hexahedral elements. The final grid model is shown in Fig. 3**c,d**. To facilitate the loading of mobility, a coupling point was established at the center of the upper surface of the intervertebral disc and coupled with the upper surface, as shown in the Figure below (Fig. 3**e,f**).

Biomechanical Analysis

The mechanical performance of the biomimetic scaffold was further evaluated from three aspects, namely displacement, strain, and stress, through finite element analysis. During the displacement simulation experiment, a slight increase in the maximum displacement of the radial hierarchical structures of the biomimetic intervertebral disc scaffold was observed during various movements such as flexion, extension, left bending, and left rotation. Significant increases were observed during left bending extension and left rotation, primarily concentrated on the upper surface of the outer annulus fibrosus (Fig. 4). In the strain and stress simulation experiments, a gradient change was found from the nucleus pulposus region to the AF 6 layer structure. In contrast, significantly higher strain and stress were observed in the AF 7 layer (outermost layer) structure (Figs. 5,6).

Morphology and Porosity of the Bio-Scaffold

The pore size of the bioscaffold microstructure is determined by the cross-linking density within the hydrogel. An appropriate pore size provides a suitable 3D microenvironment for seed cells. After the intervertebral disc hydrogel scaffold was printed and formed, three points were randomly selected on the nucleus pulposus, inner annulus fibrosus, and outer annulus fibrosus for SEM observation (Fig. 7**a–c**). The average pore sizes at the three positions were 107.76 ± 22.22 μm, 49.65 ± 9.83 μm, and 6.85 ± 1.6 μm, respectively (Fig. 7**h**). These findings indicate that the hydrogel scaffold contained a network structure with pores of different sizes in different areas, leading to different cell morphologies at different biological positions (Fig. 7**g**).

Cytoskeleton Staining

The biomimetic intervertebral disc scaffold was stained with phalloidin/DAPI, and three test points were selected on the NP, inner annulus fibrosus, and outer annulus fibrosus to observe the cytoskeleton morphology (**Fig. 7d–f**). These findings indicate variations in the distribution and morphology of cytoskeletal microtubules within the different regions of the intervertebral disc. Specifically, the nucleus pulposus exhibited relatively sparse microtubules, with cells displaying a well-spread, polygonal shape, and high fluorescence density. Conversely, the inner annulus fibrosus displayed more pronounced microtubules, with a mix of well-spread and clustered cell shapes, and medium fluorescence density. Denser microtubules were found in the outer annulus fibrosus, with the majority of cells showing a clustered shape and a lower fluorescence density. A statistically significant difference in fluorescence density was observed between the three areas ($p < 0.01$, n ≥3 (Fig. 7**i**).

Biocompatibility Assessment

The biocompatibility of the hydrogel was assessed using Calcein/PI cell viability and cytotoxicity assay kits (Fig. 8**a**). One day after incubation, the NPMSCs survival rate of the BCN hydrogel was 99.035 ± 0.13 % (Fig. 8**b**). Further incubation for four days resulted in a cell survival rate of 98.6518 ± 0.08 % (Fig. 8**c**), while the cell survival rate was 98.2584 ± 0.24 % after seven days of incubation. Statistical analysis revealed significant differences in fluorescence density among the three time points ($p < 0.01$, n ≥3). Procedures for the identification of relevant NPMSCs are described in **Supplementary Materials S1–S3**.

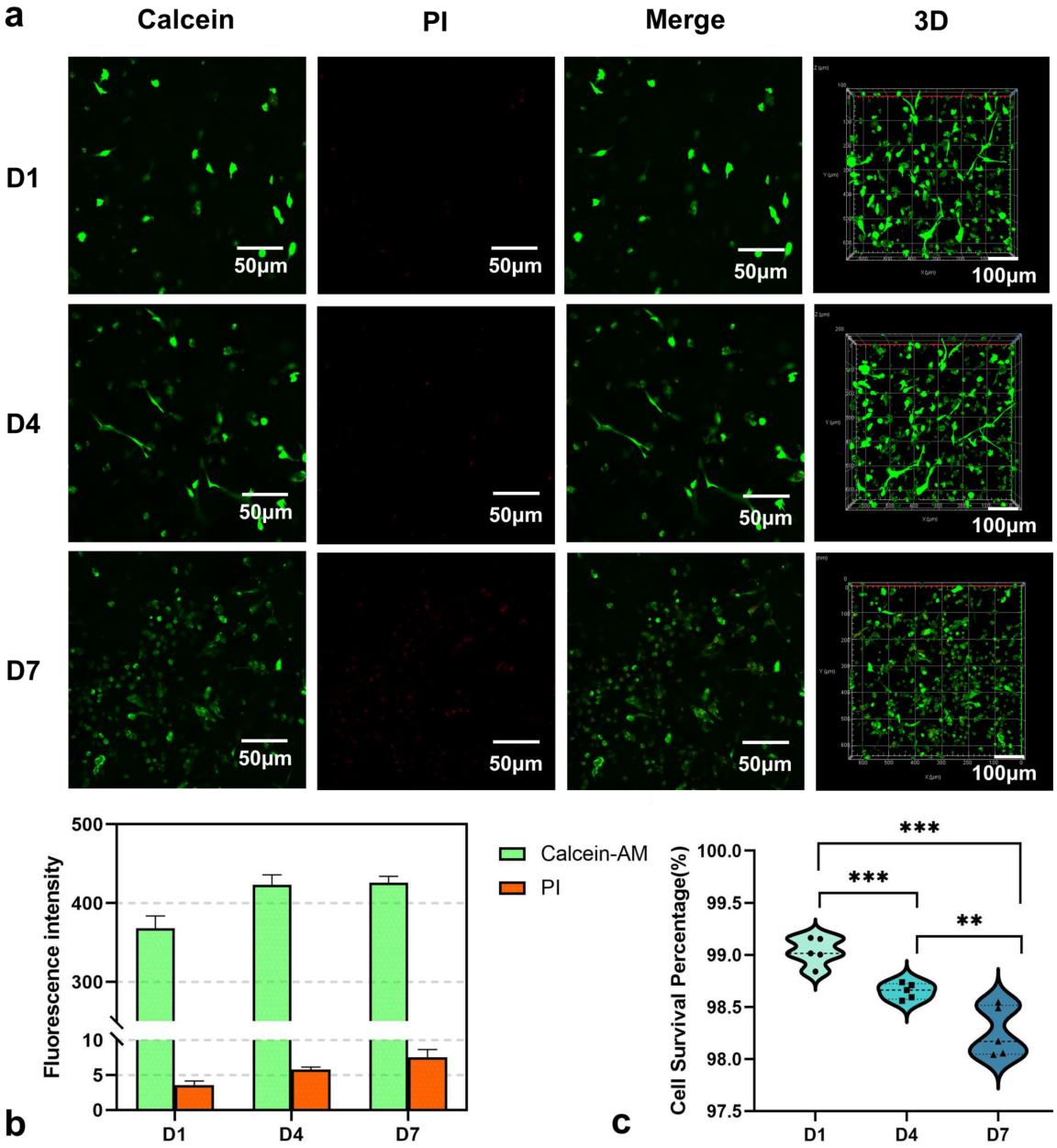

Fig. 8. Live/dead staining experiment. (**a**) Although the proportion of dead cells increases progressively from Day 1 to Day 7 (D1–D7) (2D scale bar: 50 μm, 3D scale bar: 100 μm), (**b,c**) the overall cell viability remains at a relatively high level, which confirms the good biocompatibility of the intervertebral disc bio-scaffold. All tests were conducted three times. Symbols representing significance levels are indicated as follows: $^{**}p < 0.01$, $^{***}p < 0.001$. This image was produced using GraphPad Prism software. Calcein-AM, Calcein acetoxymethyl; PI, propidium iodide.

Discussion

In this study, detailed analysis of grayscale MRI images provided accurate biomechanical parameters for distinguishing between different tissue types within the intervertebral disc. This step is required for the precise design of a biological scaffold as it allows simulation of the natural gradient structure of the intervertebral disc based on variations in tissue grayscale values. The results from the ImageJ software analysis further confirmed the radial gradient changes in the MRI images of the intervertebral disc, providing crucial data supporting the reverse calculation of exposure intensity and subsequent biological scaffold manufacturing.

GE-DLP enables precise control of the exposure intensity during the 3D printing process based on the grayscale values of the MRI images, playing an essential role in

simulating the complex structure of the intervertebral disc. The spatial distribution of light intensity was digitally encoded and precisely controlled during the DLP printing process, and a biomimetic scaffold with a gradient structure was prepared using a biocompatible BCN hydrogel as the bio-ink. Subsequently, the matrix hardness and nanostructure of the biomimetic scaffold were examined from a microscopic perspective through nanoindentation experiments and SEM. The results suggested that the elastic modulus and pore size of the biomimetic scaffold exhibited a clear gradient change from the inside to the outside in the radial direction, which is highly consistent with the ultrastructure and biomechanical characteristics of the natural intervertebral disc [33–35].

The dynamic mechanical properties of the biomimetic intervertebral disc scaffold were evaluated, and the nanoindentation experimental data obtained from the aforementioned steps were imported into the constructed three-dimensional finite element model of the intervertebral disc for thresholding and material assignment. Subsequently, the displacement changes and stress-strain distribution of the scaffold were simulated and verified under four conditions: flexion, extension, left rotation, and left lateral bending. The FEA results revealed that the biomimetic intervertebral disc scaffold exhibited a similar response to the biomechanical characteristics of the actual intervertebral disc in terms of displacement, strain, and stress, particularly during the simulation of left rotation and left lateral bending movements, where the strain and stress of the outer annulus fibers significantly increased, which is consistent with the clinically observed injury patterns [36,37].

To further verify the biocompatibility of the intervertebral disc biomimetic scaffold, NPMSCs were cultured *ex vivo* and resuspended in BCN hydrogel bio-ink for 3D bioprinting. First, specific staining of F-actin filaments was marked in the NPMSC-laden intervertebral disc scaffold using phalloidin staining. Combined with the SEM observation of the scaffold's porous structure, the biological scaffolds in different regions adopted a network structure of pores of different sizes, playing a crucial role in cell adhesion, growth, and tissue regeneration. Quantitative analysis of porosity showed significant differences in pore size among different regions, with the size of the pores displaying a positive correlation with the fluorescence density of cytoskeleton staining, further revealing differences in the distribution of cell microtubules and cell morphology in different regions. These findings may be attributed to the biomechanical functions of cells in different regions of the intervertebral disc [38].

The viability and cytotoxicity of the NPMSC-laden intervertebral disc scaffold were assessed by live-dead staining, exploring the safety and effectiveness of biological scaffolds in clinical applications. The results of the calcein/PI cell activity and cytotoxicity assays revealed that although the cell survival rate slightly decreased as the incubation time was prolonged, a high level was generally maintained, indicating good biocompatibility of the hydrogel scaffold.

Nevertheless, the limitations of the present study should be acknowledged. In this study, an intervertebral disc biomimetic scaffold was constructed but was only evaluated by *in vitro* experiments, lacking *in vivo* validation through animal experiments. Future studies should focus on conducting *in vivo* experiments to verify the findings.

In summary, our study has endeavored to develop a biomimetic intervertebral disc scaffold that respectfully attempts to emulate the natural gradient structure, biomechanical properties, cellular morphology, and biocompatibility of the intervertebral discs. We hope that this scaffold may offer a promising approach for the repair and regeneration of degenerated IVDs. The combination of MRI image processing and GE-DLP technology provides a new method for the precise construction of biological scaffolds. Multifaceted evaluations such as finite element analysis, microscopic structural observation, cytoskeleton staining, and biocompatibility assessment further verify the clinical application potential of the scaffold. These results not only provide new strategies for the treatment of intervertebral disc diseases but also offer valuable experience and insights for the development of tissue engineering and biomaterials.

Conclusions

In this study, MRI original grayscale images were combined with GE-DLP technology to construct a biomimetic biological scaffold that closely resembles a natural intervertebral disc in terms of both microstructure and mechanical properties. The biomimetic scaffold was evaluated and validated through *in vitro* studies, including biomechanical analysis, microscopic structural observation, and biocompatibility assessment. The results revealed that the intervertebral disc biomimetic scaffold fabricated using this method possessed excellent static structural integrity and biomechanical performance.

List of Abbreviations

IVD, intervertebral disc; MRI, magnetic resonance imaging; GE-DLP, gray exposure digital light processing; BCN, bicomponent polymer network; NPMSCs, nucleus pulposus mesenchymal stem cells; SEM, scanning electron microscopy; FEA, finite element analysis; NP, nucleus pulposus; IAF, inner annulus fibrosus; OAF, outer annulus fibrosus; HAMA, hyaluronic acid methacrylate; GelMA, gelatin methacrylate; UV, ultraviolet; PBS, phosphate buffered saline; HA, fibrin/hyaluronic acid; ANOVA, analysis of variance; DMD, digital micromirror device; SD, standard deviation; MR, magnetic resonance; AF, annulus fibrosus; 3D, three-dimensional; PI, propidium iodide; Calcein-AM, Calcein acetoxymethyl; DAPI, 4′,6-diamidino-2-phenylindole; LL, left lateral; LA, left axial.

Availability of Data and Materials

The raw data of microscopic images of this research are deposited to Zenodo and will be publicly available as of the date of publication. All data reported in this paper will also be shared by the lead contact upon request.

Author Contributions

YCY, CS, CCZ, YMS contributed to the conception or design of this research. YCY performed the research. YW, WJC, JX, RW, KZ contributed to the interpretation of data for the research. FGL, PS, YPN, HWY, ZCW, TM, SJ contributed to the acquisition and analysis of data. All authors were involved in drafting the work and critically reviewing it for important intellectual content. All authors gave the final approval of the version to be published. All authors contributed to editorial changes in the manuscript. All authors agreed to be accountable for all aspects of the work in ensuring that questions related to the accuracy or integrity of any part of the work were appropriately investigated and resolved.

Ethics Approval and Consent to Participate

This study was performed in line with the principles of the Declaration of Helsinki. The Institutional Animal Care and Use Committee of Bengbu Medical University approved all protocols used in this study. All animal studies were performed under an Institutional Animal Care and Use Committee-approved protocol (ID 2022KY108) at the Bengbu Medical College. All human studies were approved by the Independent Ethics Committee of Bengbu Medical University (Approval No.: 2023YJS181), and informed consent of the volunteers has been obtained.

Acknowledgments

We gratefully acknowledge the assistance and instruction from Prof. Xiaolong Wang and Dr. Tao Wu of the Lanzhou Institute of Chemical Physics.

Funding

This work was supported by the Natural Science Foundation of Anhui Province (2308085MH249), Natural Science Research Program of Anhui Provincial Department of Education (2022AH051487,2023AH051987), Health Research Program of Anhui (AHWJ2023A10058, AHWJ2023A30150), Pre research foundation of The Second Affiliated Hospital of Soochow University (SDFEYGJ2005), and Anhui Provincial Undergraduate Innovative Training Program(S202410367030).

Conflict of Interest

The authors declare no competing interests. This article has already been uploaded to a preprint (https://www.researchsquare.com/article/rs-5019488/v1).

Supplementary Material

Supplementary material associated with this article can be found, in the online version, at https://doi.org/10.22203/eCM.v051a03.

References

[1] Nikkhoo M, Wang JL, Parnianpour M, El-Rich M, Khalaf K. Biomechanical response of intact, degenerated and repaired intervertebral discs under impact loading-*Ex-vivo* and In-Silico investigation. Journal of Biomechanics. 2018; 70: 26–32. https://doi.org/10.1016/j.jbiomech.2018.01.026.

[2] Kamali A, Ziadlou R, Lang G, Pfannkuche J, Cui S, Li Z, *et al.* Small molecule-based treatment approaches for intervertebral disc degeneration: Current options and future directions. Theranostics. 2021; 11: 27–47. https://doi.org/10.7150/thno.48987.

[3] Battié MC, Videman T. Lumbar disc degeneration: epidemiology and genetics. The Journal of Bone and Joint Surgery. American Volume. 2006; 88: 3–9. https://doi.org/10.2106/JBJS.E.01313.

[4] Richardson SM, Mobasheri A, Freemont AJ, Hoyland JA. Intervertebral disc biology, degeneration and novel tissue engineering and regenerative medicine therapies. Histology and Histopathology. 2007; 22: 1033–1041. https://doi.org/10.14670/HH-22.1033.

[5] Mitchell UH, Helgeson K, Mintken P. Physiological effects of physical therapy interventions on lumbar intervertebral discs: A systematic review. Physiotherapy Theory and Practice. 2017; 33: 695–705. https://doi.org/10.1080/09593985.2017.1345026.

[6] Gkantsinikoudis N, Kapetanakis S, Magras I, Tsiridis E, Kritis A. Tissue Engineering of Human Intervertebral Disc: A Concise Review. Tissue Engineering. Part B, Reviews. 2022; 28: 848–860. https://doi.org/10.1089/ten.TEB.2021.0090.

[7] Zhao Y, Dong H, Xia Q, Wang Y, Zhu L, Hu Z, *et al.* A new strategy for intervertebral disc regeneration: The synergistic potential of mesenchymal stem cells and their extracellular vesicles with hydrogel scaffolds. Biomedicine & Pharmacotherapy = Biomédecine & Pharmacothérapie. 2024; 172: 116238. https://doi.org/10.1016/j.biopha.2024.116238.

[8] Tavakoli J, Diwan AD, Tipper JL. The ultrastructural organization of elastic fibers at the interface of the nucleus and annulus of the intervertebral disk. Acta Biomaterialia. 2020; 114: 323–332. https://doi.org/10.1016/j.actbio.2020.07.021.

[9] Steward AJ, Kelly DJ. Mechanical regulation of mesenchymal stem cell differentiation. Journal of Anatomy. 2015; 227: 717–731. https://doi.org/10.1111/joa.12243.

[10] Huang YC, Hu Y, Li Z, Luk KDK. Biomaterials for intervertebral disc regeneration: Current status and looming challenges. Journal of Tissue Engineering and Regenerative Medicine. 2018; 12: 2188–2202. https://doi.org/10.1002/term.2750.

[11] Mohd Isa IL, Mokhtar SA, Abbah SA, Fauzi MB, Devitt A, Pandit A. Intervertebral Disc Degeneration: Biomaterials and Tissue Engineering Strategies toward Precision Medicine. Advanced Healthcare Materials. 2022; 11: e2102530. https://doi.org/10.1002/adhm.202102530.

[12] Kasamkattil J, Gryadunova A, Martin I, Barbero A, Schären S, Krupkova O, *et al.* Spheroid-Based Tissue Engineering Strategies for Regeneration of the Intervertebral Disc. International Journal of Molecular Sciences. 2022; 23: 2530. https://doi.org/10.3390/ijms23052530.

[13] Shamsah AH, Cartmell SH, Richardson SM, Bosworth LA. Tissue Engineering the Annulus Fibrosus Using 3D Rings of Electrospun PCL:PLLA Angle-Ply Nanofiber Sheets. Frontiers in Bioengineering and Biotechnology. 2020; 7: 437. https://doi.org/10.3389/fbioe.2019.00437.

[14] Bhunia BK, Kaplan DL, Mandal BB. Silk-based multilayered angle-ply annulus fibrosus construct to recapitulate form and function of

the intervertebral disc. Proceedings of the National Academy of Sciences of the United States of America. 2017; 115: 477–482. https://doi.org/10.1073/pnas.1715912115.

[15] Jin X, Kang R, Deng R, Zhao X, Wang Z, Rong W, *et al*. Fabrication and characterization of an acellular annulus fibrosus scaffold with aligned porous construct for tissue engineering. Journal of Biomaterials Applications. 2021; 36: 985–995. https://doi.org/10.1177/08853282211041956.

[16] Frauchiger DA, May RD, Bakirci E, Tekari A, Chan SCW, Wöltje M, *et al*. Genipin-Enhanced Fibrin Hydrogel and Novel Silk for Intervertebral Disc Repair in a Loaded Bovine Organ Culture Model. Journal of Functional Biomaterials. 2018; 9: 40. https://doi.org/10.3390/jfb9030040.

[17] Varma DM, DiNicolas MS, Nicoll SB. Injectable, redox-polymerized carboxymethylcellulose hydrogels promote nucleus pulposus-like extracellular matrix elaboration by human MSCs in a cell density-dependent manner. Journal of Biomaterials Applications. 2018; 33: 576–589. https://doi.org/10.1177/0885328218805216.

[18] Lang G, Obri K, Saravi B, Boccaccini AR, Früh A, Seidenstücker M, *et al.* Architecture-Promoted Biomechanical Performance-Tuning of Tissue-Engineered Constructs for Biological Intervertebral Disc Replacement. Materials. 2021; 14: 2692. https://doi.org/10.3390/ma14102692.

[19] Christiani T, Mys K, Dyer K, Kadlowec J, Iftode C, Vernengo AJ. Using embedded alginate microparticles to tune the properties of *in situ* forming poly(*N*-isopropylacrylamide)-graft-chondroitin sulfate bioadhesive hydrogels for replacement and repair of the nucleus pulposus of the intervertebral disc. JOR Spine. 2021; 4: e1161. https://doi.org/10.1002/jsp2.1161.

[20] Chuah YJ, Wu Y, Chia YQ, Cheong MLS, Joshua JJN, Kang Y, *et al.* The co-influence of hyaluronic acid and collagen on the development of an engineered annulus tissue model with bone marrow stromal cells. Biomedical Materials. 2022; 17: 054101. https://doi.org/10.1088/1748-605X/ac7cac.

[21] Choy ATH, Leong KW, Chan BP. Chemical modification of collagen improves glycosaminoglycan retention of their co-precipitates. Acta Biomaterialia. 2013; 9: 4661–4672. https://doi.org/10.1016/j.actbio.2012.09.016.

[22] Kim DH, Martin JT, Gullbrand SE, Elliott DM, Smith LJ, Smith HE, *et al.* Fabrication, maturation, and implantation of composite tissue-engineered total discs formed from native and mesenchymal stem cell combinations. Acta Biomaterialia. 2020; 114: 53–62. https://doi.org/10.1016/j.actbio.2020.05.039.

[23] Jacobs NT, Cortes DH, Peloquin JM, Vresilovic EJ, Elliott DM. Validation and application of an intervertebral disc finite element model utilizing independently constructed tissue-level constitutive formulations that are nonlinear, anisotropic, and time-dependent. Journal of Biomechanics. 2014; 47: 2540–2546. https://doi.org/10.1016/j.jbiomech.2014.06.008.

[24] Jiang P, Zhang Y, Mu X, Liu D, Liu Y, Guo R, *et al*. Grayscale Stereolithography of Gradient Hydrogel with Site-Selective Shape Deformation. Advanced Materials Technologies. 2021; 7: 2101288. https://doi.org/10.1002/admt.202101288.

[25] Kuang X, Wu J, Chen K, Zhao Z, Ding Z, Hu F, *et al.* Grayscale digital light processing 3D printing for highly functionally graded materials. Science Advances. 2019; 5: eaav5790. https://doi.org/10.1126/sciadv.aav5790.

[26] Yao H, Wang J, Mi S. Photo Processing for Biomedical Hydrogels Design and Functionality: A Review. Polymers. 2017; 10: 11. https://doi.org/10.3390/polym10010011.

[27] Monteiro N, Thrivikraman G, Athirasala A, Tahayeri A, França CM, Ferracane JL, *et al*. Photopolymerization of cell-laden gelatin methacryloyl hydrogels using a dental curing light for regenerative dentistry. Dental Materials: Official Publication of the Academy of Dental Materials. 2018; 34: 389–399. https://doi.org/10.1016/j.dental.2017.11.020.

[28] Ye Y, Xu P, Li C, Jin S, Hu J, Fang Y, *et al*. Bioactive hydrogel encapsulated dual-gene engineered nucleus pulposus stem cells towards intervertebral disc tissue repair. Chemical Engineering Journal. 2023; 453: 139717. https://doi.org/10.1016/j.cej.2022.139717.

[29] Yu X, Zhao Y, Abudouaini H, Zou P, Li T, Bai X, *et al*. A novel spherical GelMA-HAMA hydrogel encapsulating APET×2 polypeptide and CFIm25-targeting sgRNA for immune microenvironment modulation and nucleus pulposus regeneration in intervertebral discs. Journal of Nanobiotechnology. 2024; 22: 556. https://doi.org/10.1186/s12951-024-02783-z.

[30] Xu P, Guan J, Chen Y, Xiao H, Yang T, Sun H, *et al*. Stiffness of photocrosslinkable gelatin hydrogel influences nucleus pulposus cell properties *in vitro*. Journal of Cellular and Molecular Medicine. 2021; 25: 880–891. https://doi.org/10.1111/jcmm.16141.

[31] Ghorbani M, Ai J, Nourani MR, Azami M, Hashemi Beni B, Asadpour S, *et al*. Injectable natural polymer compound for tissue engineering of intervertebral disc: *In vitro* study. Materials Science & Engineering. C, Materials for Biological Applications. 2017; 80: 502–508. https://doi.org/10.1016/j.msec.2017.06.007.

[32] Panjabi MM, Oxland TR, Yamamoto I, Crisco JJ. Mechanical behavior of the human lumbar and lumbosacral spine as shown by three-dimensional load-displacement curves. The Journal of Bone and Joint Surgery. American Volume. 1994; 76: 413–424. https://doi.org/doi:10.2106/00004623-199403000-00012.

[33] Nerurkar NL, Elliott DM, Mauck RL. Mechanical design criteria for intervertebral disc tissue engineering. Journal of Biomechanics. 2010; 43: 1017–1030. https://doi.org/10.1016/j.jbiomech.2009.12.001.

[34] Umehara S, Tadano S, Abumi K, Katagiri K, Kaneda K, Ukai T. Effects of degeneration on the elastic modulus distribution in the lumbar intervertebral disc. Spine. 1996; 21: 811–820. https://doi.org/10.1097/00007632-199604010-00007.

[35] Gruber HE, Hanley EN Jr. Ultrastructure of the human intervertebral disc during aging and degeneration: comparison of surgical and control specimens. Spine. 2002; 27: 798–805. https://doi.org/doi:10.1097/00007632-200204150-00004.

[36] Kos N, Gradisnik L, Velnar T. A Brief Review of the Degenerative Intervertebral Disc Disease. Medical Archives. 2019; 73: 421–424. https://doi.org/10.5455/medarh.2019.73.421-424.

[37] Desmoulin GT, Pradhan V, Milner TE. Mechanical Aspects of Intervertebral Disc Injury and Implications on Biomechanics. Spine. 2020; 45: E457–E464. https://doi.org/10.1097/BRS.0000000000003291.

[38] Zhou T, Chen Y, Liao Z, Zhang L, Su D, Li Z, *et al*. Spatiotemporal Characterization of Human Early Intervertebral Disc Formation at Single-Cell Resolution. Advanced Science. 2023; 10: e2206296. https://doi.org/10.1002/advs.202206296.

Editor's note: The Scientific Editor responsible for this paper was Bo Lei.

Received: 13th December 2024; **Accepted**: 28th March 2025; **Published**: 26th May 2025